Meteotsunamis Accompanying Tropical Cyclone Rainbands During Hurricane Harvey

Anarde, Katherine; Cheng, Wei; Tissier, Marion; Figlus, Jens; Horrillo, Juan

DOI
10.1029/2020JC016347

Publication date
2021

Document Version
Final published version

Published in
Journal of Geophysical Research: Oceans

Citation (APA)
Anarde, K., Cheng, W., Tissier, M., Figlus, J., & Horrillo, J. (2021). Meteotsunamis Accompanying Tropical Cyclone Rainbands During Hurricane Harvey. *Journal of Geophysical Research: Oceans*, *126*(1), 1-15. Article e2020JC016347. https://doi.org/10.1029/2020JC016347

JGR Oceans

RESEARCH ARTICLE
10.1029/2020JC016347

Special Section:
The Three Major Hurricanes of 2017: Harvey, Irma and Maria

Meteotsunamis Accompanying Tropical Cyclone Rainbands During Hurricane Harvey

Katherine Anarde[1,2], Wei Cheng[3], Marion Tissier[4], Jens Figlus[3], and Juan Horrillo[3]

[1]Department of Civil and Environmental Engineering, Rice University, Houston, TX, USA, [2]Now at Department of Geological Sciences, University of North Carolina at Chapel Hill, Chapel Hill, NC, USA, [3]Department of Ocean Engineering, Texas A&M University, Galveston, TX, USA, [4]Faculty of Civil Engineering and Geosciences, Delft University of Technology, Delft, The Netherlands

Abstract Meteotsunami waves can be triggered by atmospheric disturbances accompanying tropical cyclone rainbands (TCRs) before, during, and long after a tropical cyclone (TC) makes landfall. Due to a paucity of high-resolution field data along open coasts during TCs, relatively little is known about the atmospheric forcing that generate and resonantly amplify these ocean waves, nor their coastal impact. This study links high-resolution field measurements of sea level and air pressure from Hurricane Harvey (2017) with a numerical model to assess the potential for meteotsunami generation by sudden changes in air pressure accompanying TCRs. Previous studies, through the use of idealized models, have suggested that wind is the dominant forcing mechanism for TCR-induced meteotsunami with negligible contributions from air pressure. Our model simulations show that large air pressure perturbations (~1–3 mbar) can generate meteotsunamis that are similar in period (~20 min) and amplitude (~0.2 m) to surf zone observations. The measured air pressure disturbances were often short in wavelength, which necessitates a numerical model with high temporal and spatial resolution to simulate meteotsunami triggered by this mechanism. Sensitivity analysis indicates that air pressure forcing can produce meteotsunami with amplitudes *O(0.5 m)* and large spatial extents, but model results are sensitive to atmospheric factors, including model uncertainties (length, forward translation speed, and trajectory of the air pressure disturbance), as well as oceanographic factors (storm surge). The present study provides observational and numerical evidence that suggest that air pressure perturbations likely play a larger role in meteotsunami generation by TCRs than previously identified.

Plain Language Summary During tropical cyclones, spiral rainbands distant from the storm center can trigger ocean waves with periods similar to tsunami but created by atmospheric processes. These meteorological tsunami ("meteotsunami") waves are generated by large increases in wind speeds and/or drops in air pressure as the spiral rainbands pass over the ocean. The waves can grow in height when the speed of the wind or air pressure disturbance matches the speed of the forced ocean wave. The current scientific understanding is that wind is the key factor that enables these waves to grow in height. However, relatively little is known about the air and wind forcing that trigger meteotsunami nor the beach hazards they pose as it is challenging to collect field data during storm impact. In this study, we combine new field measurements and a numerical model to show that that sudden and sharp changes in air pressure can also enable meteotsunami to grow in height. Simulations show that these waves can reach up to 1 m in height, and therefore present a significant beach hazard, but the size depends on oceanographic and storm-specific factors, including the amount of storm surge.

Key Points:

- Modeling suggests air pressure anomalies accompanying rainbands can trigger meteotsunamis similar to observations
- High spatio-temporal resolution is needed to simulate sudden changes in air pressure and ensuing meteotsunami
- Meteotsunami size and extent is dependent on atmospheric and oceanographic factors, including storm surge

Supporting Information:

- Supporting Information S1
- Movie S1
- Movie S2

Correspondence to:
K. Anarde,
kanarde@unc.edu

Citation:
Anarde, K., Cheng, W., Tissier, M., Figlus, J., & Horrillo, J. (2021). Meteotsunamis accompanying tropical cyclone rainbands during Hurricane Harvey. *Journal of Geophysical Research: Oceans*, *126*, e2020JC016347. https://doi.org/10.1029/2020JC016347

Received 24 APR 2020
Accepted 2 DEC 2020

1. Introduction

Observational evidence has shown that tropical cyclones (TCs) can initiate ocean waves with periods similar to tsunami (several minutes to hours) but created by atmospheric processes rather than by seismic or other sources (e.g., landslides) (Dusek et al., 2019; Lin & Wu, 2020; Mecking et al., 2009; Mercer et al., 2002; Olabarrieta et al., 2017; Shi et al., 2020). Tide gauge records indicate that meteorological tsunamis ("meteotsunamis") are particularly common in the Gulf of Mexico (GOM) and along Florida's Atlantic Coast during TCs, the largest of which measured 0.78 at the Freshwater Canal Locks in Louisiana during Hurricane Harvey (2017) (Shi et al., 2020). During this storm, tide gauge records along much of the Texas coast showed variability in the meteotsunami frequency band before, during, and after landfall, indicating that

meteotsunami hazard can extend several days before and after hurricane landfall (Shi et al., 2020). In the GOM, TC-induced meteotsunami are thought to be initiated by substorm-scale atmospheric features, namely air pressure and wind disturbances accompanying tropical cyclone rainbands (TCRs) (Shi et al., 2020). These ocean waves present a flood hazard through their slow, and often unexpected, increase in total water level, beyond what is predicted for storm surge. TC-induced meteotsunami may also represent a beach hazard through initiation of extreme wave runup (e.g., as during the Daytona Beach 1992 meteotsunami; Churchill et al., 1995), generation of rip currents (e.g., as in the Great Lakes; Linares et al., 2019), or by contributing to morphological change (dune and beach erosion). However, given the sheltered locations of tide gauges (i.e., within estuaries, harbors, and bays), and scarcity of field data close to shore during extreme events, relatively little is known about meteotsunami hazard along open coasts during TCs.

Meteotsunami generation on open coasts is typically a multiresonant process (Monserrat et al., 2006). First, sudden changes in air pressure and/or wind associated with a moving atmospheric disturbance (e.g., storm, squall, frontal passage, or atmospheric gravity wave) force a small water level perturbation (e.g., due to the inverse barometer effect). This forced wave can become strongly amplified as it propagates with the disturbance that triggered it, first due to external resonance processes and later as a free wave due to nearshore wave transformations (shoaling, refraction, and superposition of incident and reflected waves). Maximum energy transfer from the atmosphere to the ocean occurs when the speed of the disturbance approaches the shallow water wave celerity (Froude number near 1), a phenomenon called Proudman resonance (Proudman, 1929). Upon reaching the coast, additional resonance effects, such as the matching of harbor seiche periods, are required for the free wave to reach destructive heights (up to several meters)—a phenomenon that has been observed in coastal basins around the world (Rabinovich, 2020).

Using a coupled oceanic and atmospheric modeling framework, Shi et al. (2020) simulated translation of an idealized TC over a simplified shelf bathymetry and found that wind forcing alone could trigger TCR-induced meteotsunamis of similar period (1–2 h), amplitude (~0.2–0.4 m), and sequence (single peak or sequential meteotsunami) to tide gauge observations. Single peak meteotsunamis were found to be driven by "outer" TCRs—that is, rainbands that are distant from the inner core of the hurricane—and sequential meteotsunamis by trains of principal and secondary rainbands ("inner" TCRs) within the inner core region. The generation and growth of TCR-induced meteotsunamis were shown to be sensitive to bathymetry as well as TCR characteristics, including the forward translation speed, strength of the atmospheric disturbance, and trajectory. Notably, when using only pressure forcing, the modeled sea-level anomalies generally followed the inverse barometer effect and were not amplified through resonance processes.

Detailed (spatio-temporal) surface observations of the atmospheric disturbances that accompany land-falling TCRs are scarce (e.g., Hamuro et al., 1969; Ligda, 1955; Ushijima, 1958; Yu & Tsai, 2010), and no study has tested the generation potential of TCR-induced meteotsunami by measured atmospheric (air pressure or wind) forcing. Here, we analyze radar reflectivity observations and temporally high-resolution observations of surface air pressure and sea level in the nearshore environment during Hurricane Harvey. Surf zone and back-barrier sea levels showed variability in the meteotsunami frequency band (here, ~8–45 min periods) during passage of outer TCRs (maximum peak-to-trough wave height of 0.42 m). Colocated observations of air pressure indicate that the TCRs were accompanied by wave-like air pressure disturbances with large trough O(1–2.8 mbar) and peak O(1–2 mbar) amplitudes. Air pressure disturbances with similar amplitudes have been shown to be the key atmospheric forcing mechanism for meteotsunamis in the GOM during winter storms (Shi et al., 2019). Hence, in the present study, we test the alternative hypothesis that meteotsunami can be initiated and subsequently amplified by air pressure disturbances accompanying TCRs. We use a numerical model to translate simplified representations of two air pressure disturbances measured during Hurricane Harvey, which differ both in waveform and larger TCR characteristics, over realistic bathymetry. We find that the oscillations these air pressure disturbances create become amplified across the wide GOM continental shelf through Proudman resonance and can have similar peak and trough amplitudes to the sea-level anomalies observed in the surf zone (~0.2 m). We then use the model in an exploratory fashion to illustrate the sensitivity of meteotsunami generation, amplification, and propagation to oceanographic factors (storm surge) and model uncertainties (i.e., atmospheric factors including the length, forward translation speed, and trajectory of the air pressure disturbance).

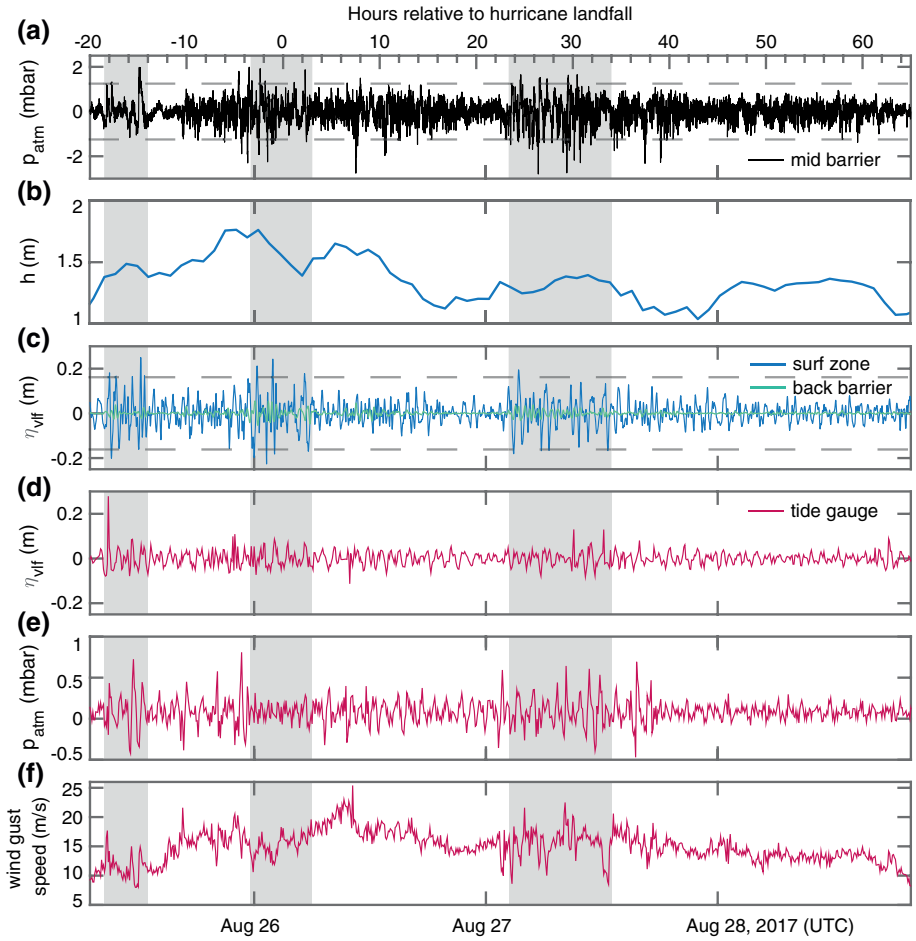

Figure 1. Full time series of (a) high-frequency air pressure p_{atm}, (b) mean-water depth h, and (c) very-low frequency (VLF) sea-level anomalies η_{vlf} in the surf zone and back-barrier at the Follets Island field site; (d) η_{vlf}, (e) p_{atm}, and (f) wind gust speed measured at NOAA tide gauge 8772471 located within Freeport harbor (NOAA, 2017). Note the different plot scales in (a) and (e). The dashed lines in (a and c) denote 3-standard deviations (σ) for p_{atm} (Follets Island) and η_{vlf} (surf zone only). Shaded intervals reflect time periods with sequential instances of η_{vlf} (surf zone) above the 3σ threshold.

2. Observations

Continuous measurements of sea level from two nearshore environments along the Texas coast showed variability at frequencies f below infragravity waves ($f < 3$ mHz, > 5.6 min periods), but above known tidal constituents and storm surge ($f > 0.1$ mHz, < 2.8 h periods) episodically during Hurricane Harvey. At the field site closest to landfall, very-low frequency ("VLF"; 5.6 min to 2.8 h periods) wave phenomena were observed to modulate infragravity waves during overwash (Anarde et al., 2020). Herein, we focus on field measurements collected farther up the coast at Follets Island (~200 km northeast of hurricane landfall) where VLF oscillations were observed in the surf zone and back barrier over a period of ~4 days (Figure 1c). Sea-level fluctuations with periods upwards of 10 min have been observed in surf zones on beaches elsewhere, with generation mechanisms typically attributed to shear instability of the alongshore current (Oltman-Shay et al., 1989) or forcing from wave groups (Haller et al., 1999) (i.e., shear waves). The VLF sea-level anomalies observed in the surf zone during Hurricane Harvey were relatively large (maximum peak-to-trough wave height = 0.42 m, Figure 2c) and much lower in frequency and span a larger frequency range (~8–45 min periods) than is typical of shear waves, suggesting an alternative or additional generation mechanism(s).

As shown in Figure 1 for the full 4-day time series and in Figure 2 for three 5-h subsets, relatively large sea-level anomalies (η) were observed at VLF (subscript vlf) during three time intervals at the Follets Is-

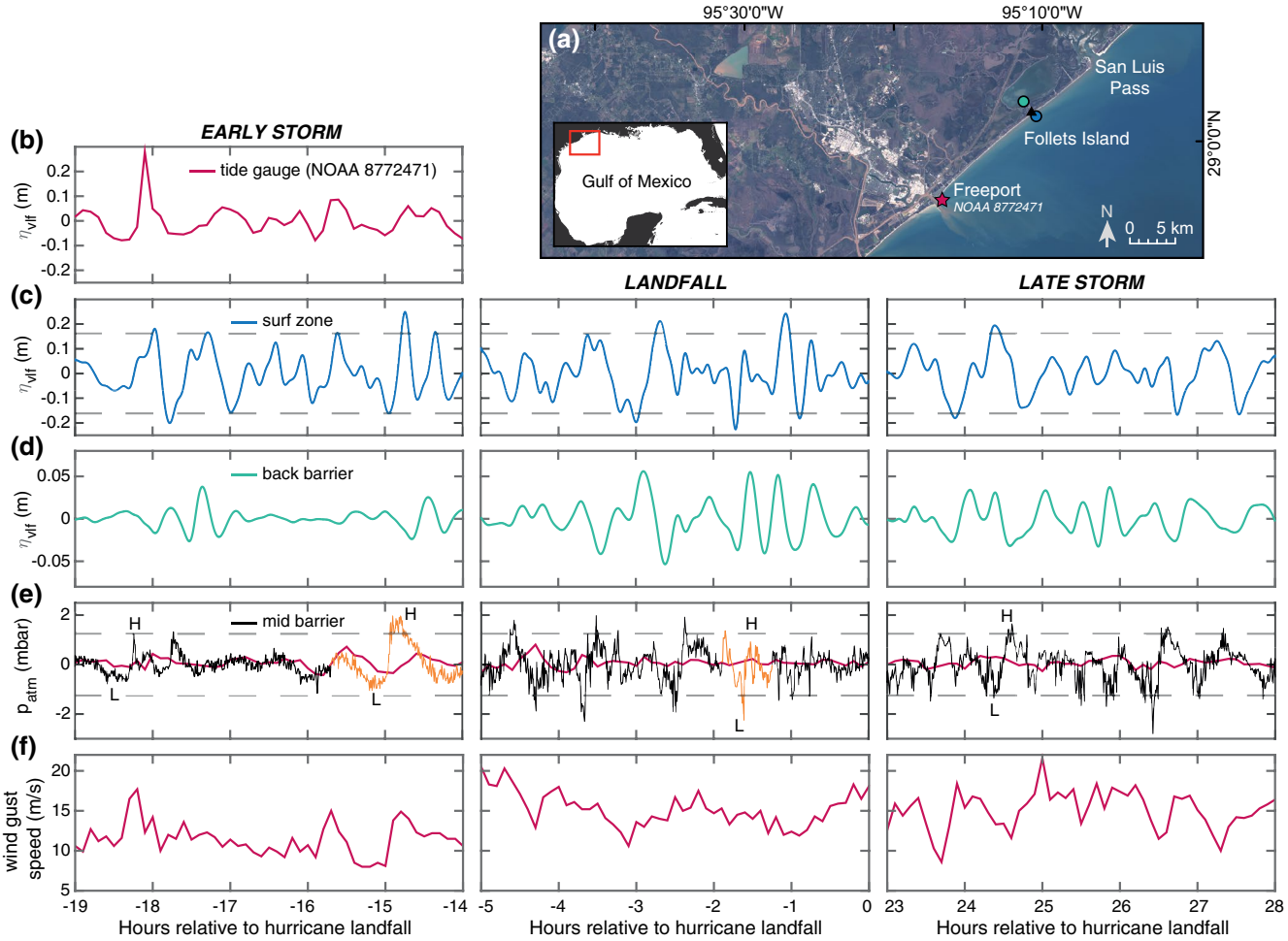

Figure 2. (a) Field site location and 5-h subsets of the (b–d) VLF sea-level anomaly η_{vlf}, (e) high-frequency air pressure p_{atm} ($f > 0.1$ mHz), and (f) wind gust speed measured at the Freeport tide gauge (NOAA 8772471) and in the surf zone and back barrier at the Follets Island field site for three time periods during the storm. The dashed lines in (c and e) denote 3-standard deviations (σ) for η_{vlf} and p_{atm} (respectively). Herein, air pressure disturbances are defined as pressure couplets with a peak ("H") or trough ("L") amplitude that exceeds 3σ (±1.25 mbar); those identified in (e) correspond to time periods in 3. The disturbances highlighted orange are used for numerical modeling.

land field site: −18.5 to −14 h ("early storm"), −3 to 3 h ("landfall"), and 23.5 to 34 h relative to hurricane landfall ("late storm"). These time periods were identified by sequential instances of η_{vlf} in the surf zone that exceeded (in absolute value) a threshold of three times the standard deviation (σ) of η_{vlf} (dashed lines, Figures 1c and 2c), where time series were bandpass filtered with a low-frequency cutoff of 0.1 mHz (2.8 h) and high-frequency cutoff of 3 mHz (5.6 min) to isolate η_{vlf}. While arbitrary, this threshold (0.16 m) allows for a more targeted examination of forcing mechanisms responsible for generation of the largest VLF oscillations. Relatively large instances of η_{vlf} were also observed in the back barrier during each of these time periods, albeit these sea-level anomalies were small in magnitude (<5 cm). Notably, the back-barrier environment was only hydraulically connected to the nearshore through a tidal inlet located 8 km northeast of the field site (San Luis Pass, Figure 2a) and via the Freeport harbor located 15 km southwest of the site for the duration of the storm (i.e., no storm overwash or island breaching occurred in the vicinity of the site). Tide gauges operated by the National Oceanic and Atmospheric Administration (NOAA) within Freeport harbor and at San Luis Pass (not shown) also showed water level variability at VLF, however, only the Freeport harbor gauge measured a VLF anomaly of similar magnitude to the surf zone oscillations (0.35 m in height at −18 h, Figures 1d and 2b).

High-resolution measurements of atmospheric (barometric) surface pressure recorded by a subaerial mounted pressure transducer in the mid-barrier environment at the Follets Island field site (30 s sampling

frequency) revealed that 87% of the 3σ exceedances of $|\eta_{vlf}|$ (surf zone) were preceded within 30 min by air pressure disturbances. An air pressure disturbance is here defined as an alternating low-to-high pressure couplet with a peak or trough amplitude that exceeds |±1.25| mbar (dashed lines in Figures 1a and 2e). This threshold defines three standard deviations of the high-frequency air pressure p_{atm}—that is, the barometric pressure high-pass filtered to remove signals representative of the inverted barometer effect associated with the storm-scale tropical depression (i.e., storm surge $f < 0.1$ mHz). As elaborated upon below, this definition allows for analysis of temporal changes in meteorological forcing throughout the study period. Notably, time series of high-frequency air pressure measured at the Freeport tide gauge (6-min sampling frequency) did not show pressure anomalies in excess of ±1.25 mbar.

On a more regional scale, mosaics of Next Generation Weather Radar reflectivity observations (a measure of precipitation intensity, Figure 3) show that air pressure disturbances measured during each of the three time periods of elevated η_{vlf} at Follets Island were often concomitant with passage of strong convective cells (>∼50 dBZ) embedded within TCRs (>∼30 dBZ) (the reader is directed to Hence & Houze, 2008 for more details on convective-scale elements in TCRs). For all three time periods, these convective cells traveled radially as part of larger TCRs past the field site. However, the direction of TCR translation (from first identification in deep water, circles in Figure 3) and orientation of the TCRs and embedded convective cells relative to the coastline differed for each time period as the TC moved landward. Early in the storm (−18.5 to −14 h), Follets Island was located in the upper right quadrant of the TC, approximately 300 km NE of the TC eyewall (Figures 3a and 3b). The land-falling TCRs at the field site during this period were infrequent, large (spanning much of the central Texas coast, >100 km in arc-length), and spiraled toward the WNW such that were oriented shore-parallel across much of the continental shelf. As the TC moved onshore (eyewall ∼200 km SW), the TCRs became oriented approximately shore-perpendicular and sequential trains of convective cells with small horizontal scales (<50 km in arc-length, −3 to 3 h, Figure 3c), passed frequently over the field site (typically every ∼30 min), traveling toward the NW. After landfall, the storm was stalled inland, and the TCRs became oriented more oblique to the coastline (23.5–34 h, Figure 3d) such that cells with intense convection and small horizontal scales (<75 km) traveled to the NE across the shelf and past the field site. The forward translation speed of the TCRs across the continental shelf during each of the three time periods was highly variable, ranging from 6 to 29 m/s along the path of a single TCR (as estimated from the reflectivity mosaics). However, the mean forward speeds of the land-falling TCRs shown in Figure 3 were similar (14–17 m/s). Note that we classify the TCRs observed during all three time periods as "outer" TCRs as they are located far outside the inner core region—that is, beyond three times the radius of maximum wind as defined by Wang (2009).

Surface pressure fluctuations of land-falling TCRs are often characterized by leading pressure troughs followed by pressure peaks, or alternatively low-to-high pressure couplets (e.g., Hamuro et al., 1969; Ligda, 1955; Ushijima, 1958; Yu & Tsai, 2010). These pressure fluctuations are likely the manifestation of atmospheric waves that are initiated close to the TC center (e.g., inertia-gravity waves Diercks & Anthes, 1976; Kurihara, 1976; Willoughby, 1977) with contributions from moist convection (Yu & Tsai, 2010). Atmospheric gravity waves produced by TCs generally have wavelengths ranging from tens to hundreds of kilometers (Kim et al., 2009), albeit gravity waves with smaller scales (radial wavelengths of 2–20 km) have also been recently observed to produce surface pressure fluctuations hundreds of kilometers from the TC center (Nolan & Zhang, 2017). The troughs (peaks) of the air pressure disturbances that were concomitant with passage of the TCRs shown in Figure 3 at Follets Island are delineated with an "L" ("H") in Figure 2e. Given that air pressure was only measured at a single point and passing TCRs and embedded convective cells were sometimes small in scale, the measured peak and trough amplitudes of the pressure couplets may be underestimated (i.e., the TCR and accompanying air pressure disturbance did not pass directly over the field site). Regardless, there is clearly a significant increase in the number of air pressure disturbances (3σ exceedances) for the period proximate to hurricane landfall over early storm conditions, a result of more frequent passage of trains of embedded convective cells. The air pressure disturbances proximate to landfall are also characterized by larger pressure trough amplitudes and shorter trough periods than the more infrequent outer TCRs typical of early storm conditions.

For the air pressure disturbances highlighted orange in Figure 2e, which are herein denoted the "early storm" and "landfall" disturbances, radar reflectivity mosaics show that the TCRs (and embedded convec-

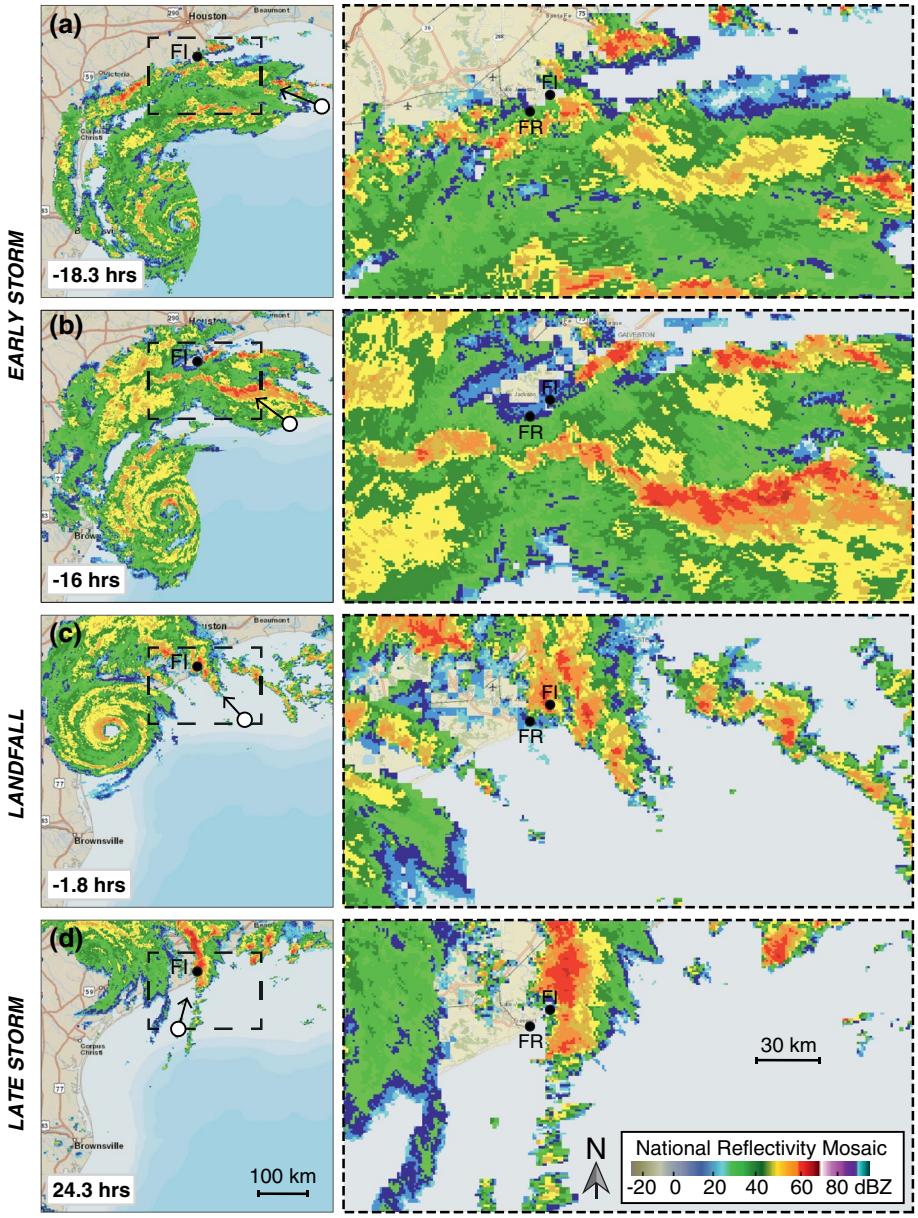

Figure 3. Next Generation Weather Radar reflectivity mosaics generated by the NOAA National Center of Environmental Information (NCEI-NOAA, 2019) showing bands of high reflectivity associated with land-falling tropical cyclone rainbands (TCRs) preceding instances of elevated η_{vlf} (above the 3σ threshold) during the a-b) "early storm", c) "landfall", and d) "late storm" time periods identified in Figure 1c (and highlighted in Figure 2). Note that the plots on the right depict the TCRs shown in the left at a finer resolution proximate to the Follets Island (FI) field site and the Freeport harbor tide gauge (FR). The circle and arrow symbols show the direction of translation of the land-falling TCRs from first identification in deep water.

tive cells) traversed directly over the Follets Island field site (Figures 3b and 3c). In the following section, we employ a numerical model to assess the generation potential of meteotsunami by a simplified representation of these air pressure disturbances, which notably differ from each other in period ("early storm"—51 min; "landfall"—21 min), trough (1 mbar; 2.25 mbar) and peak amplitudes (1.9 mbar; 0.9 mbar), as well as larger TCR characteristics (radial arc-length, trajectory). The model is then used in an exploratory framework to illustrate the sensitivity of meteotsunami generation, amplification, and propagation to model uncertainties (e.g., atmospheric factors including forward speed and trajectory) and oceanographic factors (storm surge).

3. Modeling Sea-Level Response to Air Pressure Disturbances

The numerical model utilized in this study is a 2D (depth-integrated) hydrostatic model in spherical coordinates built on the nonlinear shallow water equations, modified to include spatially dependent air pressure. The governing equations, staggered grid setup, and numerical solution scheme are outlined in Kowalik et al. (2005). The modeling domain encompasses the continental shelf along the northwestern GOM and extends landward to include harbors and bays within the greater Freeport and Houston/Galveston region (Figure 4). Bathymetry data were created with a base layer of the NOAA Etopo1 data set (Amante & Eakins, 2009) interpolated to a grid resolution of 6 arcseconds (~185 m) and referenced to the mean high water. This grid spacing was selected to achieve reasonable simulation time, while satisfying the requirement of having at least 20 grid points to numerically represent the wavelength of the air pressure disturbance. For the Freeport area (28.75–29.25 N, −95.5 to −95 W), the baseline grid is superimposed by a 1/9 arcsecond grid (NCEI, 2015) averaged to 6 arcseconds, which allows for high resolution of bathymetric variability within the Freeport Harbor, albeit subaerial structures such as the Freeport jetties are not resolved. The still water level was modified to incorporate the effect of storm surge on water depth for select simulations herein. Storm surge was estimated using the Coastal Emergency Risks Assessment web mapper tool (ADCIRC Surge Guidance System [Fleming et al., 2008], National Hurricane Center's best track) for a node offshore the field site (20 m water depth) during passage of both disturbances. Bottom friction is based on the Manning model with a Manning coefficient of 0.025 $sm^{(1/3)}$. A coastal wall is set at a water depth of 0.3 m to avoid runup on the ~185-m wide land cells. Outflow boundary conditions are applied to all the boundaries of the model domain. Model outputs are recorded at the Follets Island surf zone measurement location and the Freeport harbor tide gauge every 20 s. Astronomical tides are not included in the computations.

Due to a lack of detailed spatial information on the air pressure disturbances, it is unclear if the disturbances have the same (radial) length and shape as the radar reflectivity signal. Here, we assume a surface pressure function where the amplitude of the crest A_c and trough A_t decay exponentially along the length L of the TCR:

$$P(x,y) = \begin{cases} A_c * x * exp\left(-(y)^2 - \left(\frac{x}{L_c}\right)^2\right), x < 0 \\ A_t * x * exp\left(-(y)^2 - \left(\frac{x}{L_t}\right)^2\right), x > 0 \end{cases} \quad (1)$$

where (x, y) are the longitude and latitude excursions along L (estimated from radar reflectivity) and L_c and L_t are the wavelength of the pressure crest and trough, respectively. We create a simplified representation of the air pressure disturbances highlighted orange in Figure 2e by combining several individual pressure crests and trough waveforms, each developed using Equation 1, into a smooth continuous sequence. Values of A_c and A_t are taken directly from observations. We translate the measured duration T_c and T_t of individual peaks and troughs into wavelengths L_c and L_t using forward translation speeds U estimated from radar reflectivity observations (i.e., $L_c = T_c * U$). This results in L_c (L_t) between 27 and 37 km (28 and 63 km) for the "early storm" pressure waveform and as discussed in more detail below, between 7 and 16 km (6 and 15 km) for the "landfall" pressure waveform due to variable simulated forward speeds. Although the path of a TCR is generally radial, the translation of the pressure disturbance is here simplified to a linear path (single direction) beginning at the edge of the continental shelf and extending inland past the Follets Island field site.

3.1. Sensitivity to Disturbance Length, Forward Speed, and Trajectory

Figure 4 provides an overview of the processes responsible for meteotsunami generation, amplification, and propagation in the numerical simulations, illustrated for the "early storm" disturbance translating with a forward speed of 21 m/s and 0.56 m of storm surge. In deep water, the air pressure disturbance acts on the water surface following the inverse barometer effect: the high-pressure peaks force depressions in sea level and the low-pressure troughs allow sea level to rise. In contrast to storm surge generation (low pressure acting over large oceanic regions), the resulting sea-level anomaly η is small, on the order of several

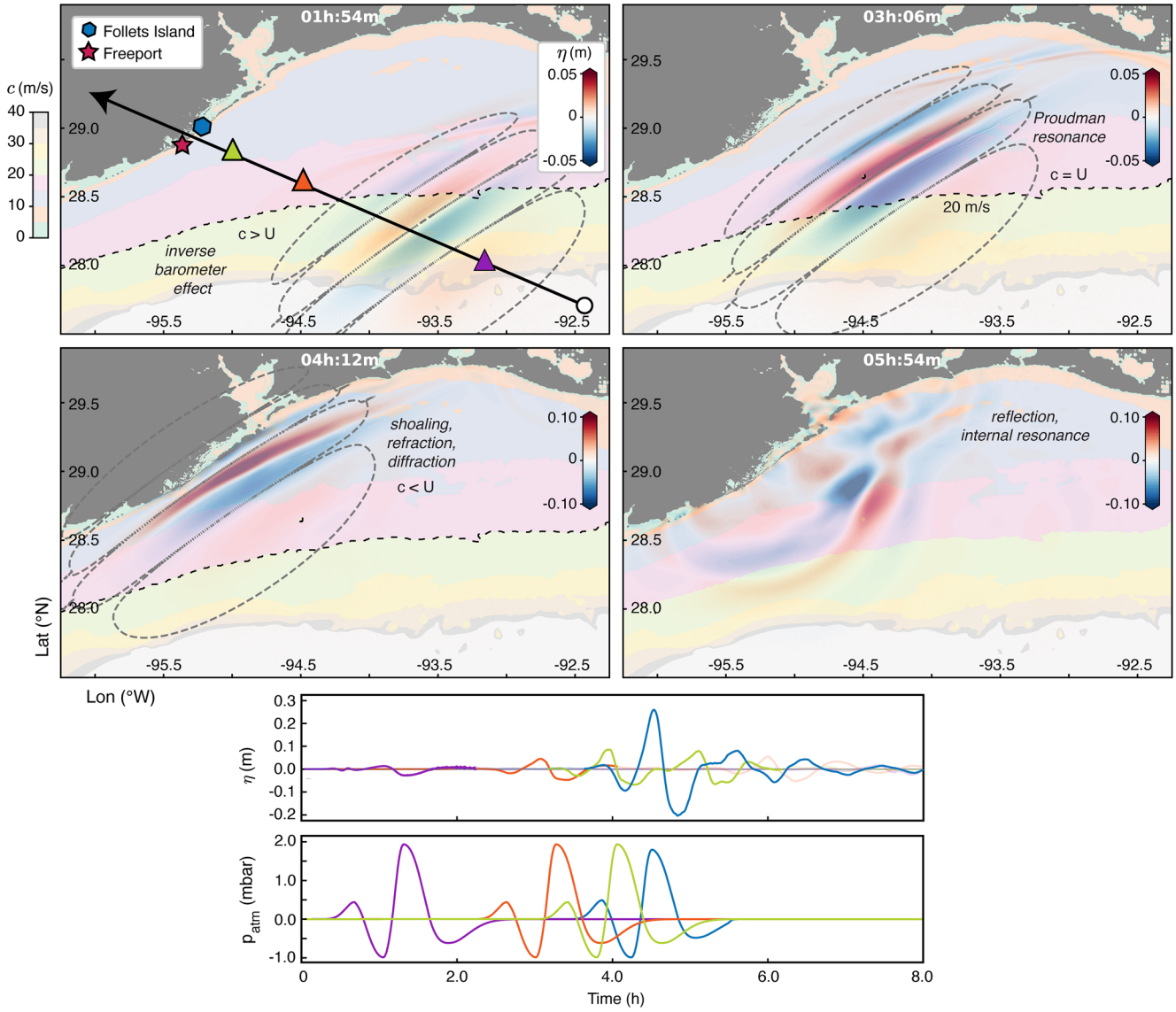

Figure 4. Overview of the model domain and processes responsible for meteotsunami generation, amplification, and propagation in the model, shown for the "early storm" air pressure disturbance p_{atm} (Figures 2e and 3b). The colored contours represent the shallow water wave celerity $c = \sqrt{gh}$ in terms of the water depth h and the blue-red colormap the instantaneous sea-level anomaly η. The bold dashed contour line identifies the location of Proudman resonance—that is, when the speed of the air pressure disturbance U matches c—and maximum energy transfer (here, 21 m/s); the solid black line shows the path along which the disturbance travels (offshore to onshore); and the dashed gray lines indicate the spatial extent of the pressure disturbance. Time series at select offshore recording stations are also shown to illustrate wave transformation across the continental shelf.

centimeters. The celerity of the sea-level anomaly (i.e., the Proudman resonance contours) is faster than the speed of the disturbance in this region (>41 m water depth). As the air pressure disturbance travels across the shelf, the forced sea-level anomaly can grow in height due to Proudman resonance. The forward speed of the air pressure disturbance determines the region (water depth) where resonant amplification occurs. Maximum energy transfer occurs when the speed of the air pressure disturbance matches the shallow water wave celerity c of the region, which in Figure 4 is delineated by a dashed bathymetry contour corresponding to a shallow water wave celerity of 21 m/s (41-m depth). Importantly, the contour of Proudman resonance also demarcates the detachment location at which the resonantly amplified wave becomes slower than the air pressure disturbance and can thereafter propagate as a free wave. The resonantly amplified wave is further transformed in the coastal zone through processes such as shoaling, refraction, diffraction, and reflection. Collectively, these processes produce a meteotsunami wave with a maximum crest elevation

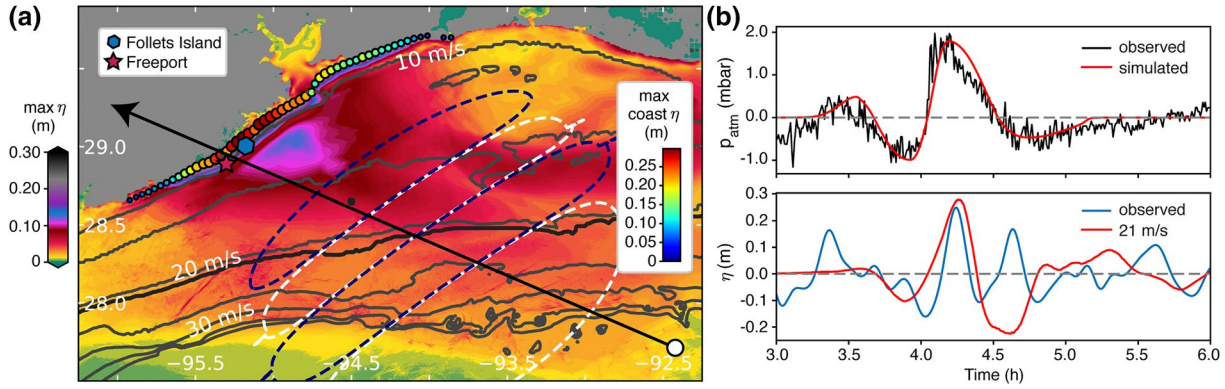

Figure 5. (a) The maximum sea-level anomaly η generated by the "early storm" air pressure disturbance p_{atm} simulated at a forward translation speed of 21 m/s across the continental shelf (colormap), along the coast (colored circles), and (b) in the surf zone at Follets Island. Time series of observed air pressure and very-low frequency (VLF) sea level at Follets Island are shown for comparison. The bold contour line in (a) identifies the location of Proudman resonance.

(herein referred to as the "maximum sea-level anomaly") of 0.28 m (peak-to-trough height of 0.52 m) in the surf zone at Follets Island and sea-level anomalies > 0.15 m along much of the upper Texas coast (Figure 5). Although radar reflectivity measurements indicate that the forward translation speed of the corresponding TCR varied across the continental shelf, 21 m/s best matched the observed lag between passage of the air pressure disturbance (pressure trough) and arrival of the peak VLF sea-level anomaly at Follets Island. Figure 5b shows that the amplitude of the simulated meteotsunami is in good agreement with the observed VLF sea-level anomaly, albeit the period is slightly overpredicted. Movie S1 in the supporting information shows an animation of the processes detailed above for the "early storm" simulation.

Estimates of TCR forward speed from radar reflectivity suggest that the TCR concomitant with passage of the "landfall" air pressure disturbance decreased in speed across the shelf, from approximately 29 to 6 m/s. With regard to meteotsunami generation, the forward speed of the atmospheric disturbance determines the depth and location of Proudman resonance and therefore is a key factor in the growth and trajectory of TCR-induced meteotsunami (Shi et al., 2020). Here we simulate the sea-level response to the "landfall" air disturbance traveling continuously over the shelf at three example forward translation speeds: 13, 17, and 25 m/s (Figures 6a–6c). Movie S2 in the supporting information shows the animation for the 17 m/s scenario. For the bathymetry and shelf morphology offshore Follets Island, forward translation speeds above 17 m/s (the mean forward speed) allow the resonantly amplified wave to detach from the air pressure disturbance far offshore and thereafter propagate toward Freeport. Note that in order to match the period of the simulated air pressure disturbance with field observations, the wavelength of the disturbance was varied for each forward speed simulation (see the changing spatial extent of the dashed lines in Figures 6a–6c). The largest simulated meteotsunami occurs for the air pressure disturbance traveling at 17 m/s (Figure 6b, 0.55 m), however the observed lag between passage of the pressure trough and arrival of the peak VLF sea-level anomaly (at 1.9 h) best matches the 25 m/s forward speed scenario (Figures 6c and 6f). Because resonance occurs far offshore for an air pressure disturbance traveling at 25 m/s, small variations in the trajectory of this disturbance, as illustrated by a 10° clockwise rotation in Figure 6e, can result in a large change in meteotsunami amplitude along the coast (i.e., a decrease in η from 0.48 to 0.32 m) due to complexities in offshore bathymetry that alter the path of meteotsunami propagation. Interestingly, the trough of the observed VLF sea-level anomaly at Follets Island at 1.3 h is in good agreement with the depression forced by the air pressure disturbance (high-pressure peak) traveling at 13 m/s, albeit the subsequent rise in sea level (by the low-pressure trough) is overpredicted. As elaborated upon below, this finding may be the result of the air pressure disturbance slowing down as it approaches land.

Although radar reflectivity mosaics show that land-falling TCRs late in the storm did not pass directly over the field site (e.g., at 24 h in Figure 3d), the waveforms of measured air pressure disturbances were similar to those observed proximate to landfall (Figure 2e). Therefore, we examine the pattern of meteotsunami growth and propagation in Figure 6d for a similar NE trajectory as a proxy. Along this trajectory the dis-

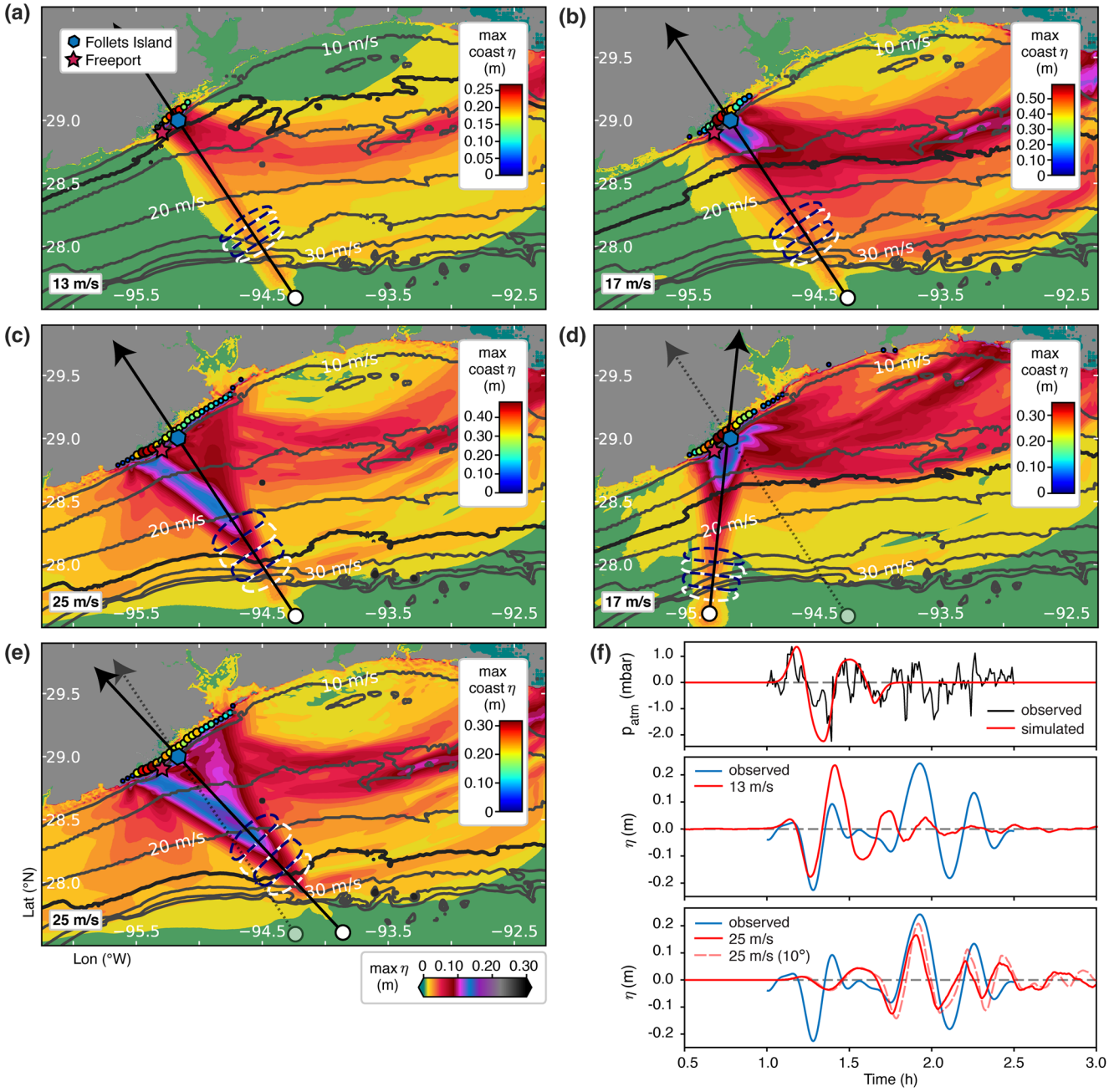

Figure 6. The maximum sea-level anomaly η generated by the "landfall" air pressure disturbance p_{atm} (Figures 2e and 3c) for simulations with variable (a–c) forward translation speeds (within the range estimated from radar reflectivity mosaics), and (d–e) trajectories across the shelf. The colormaps (colored circles) in (a–e) show the maximum η across the continental shelf (along the coast). Time series in (f) show η simulated in the surf zone at Follets Island for select scenarios, as well as the observed p_{atm} and very-low frequency (VLF) sea level for comparison.

turbance is oriented oblique to the coastline and offshore bathymetry, and as a result, produces a smaller meteotsunami amplitude along the coast, albeit a slightly larger spatial extent.

3.2. Sensitivity to Storm Surge

Hurricane Harvey was a relatively minor surge event; for the two time periods encompassing the "early storm" and "landfall" air pressure disturbances, the estimated storm surge ζ offshore Follets Island was 0.56

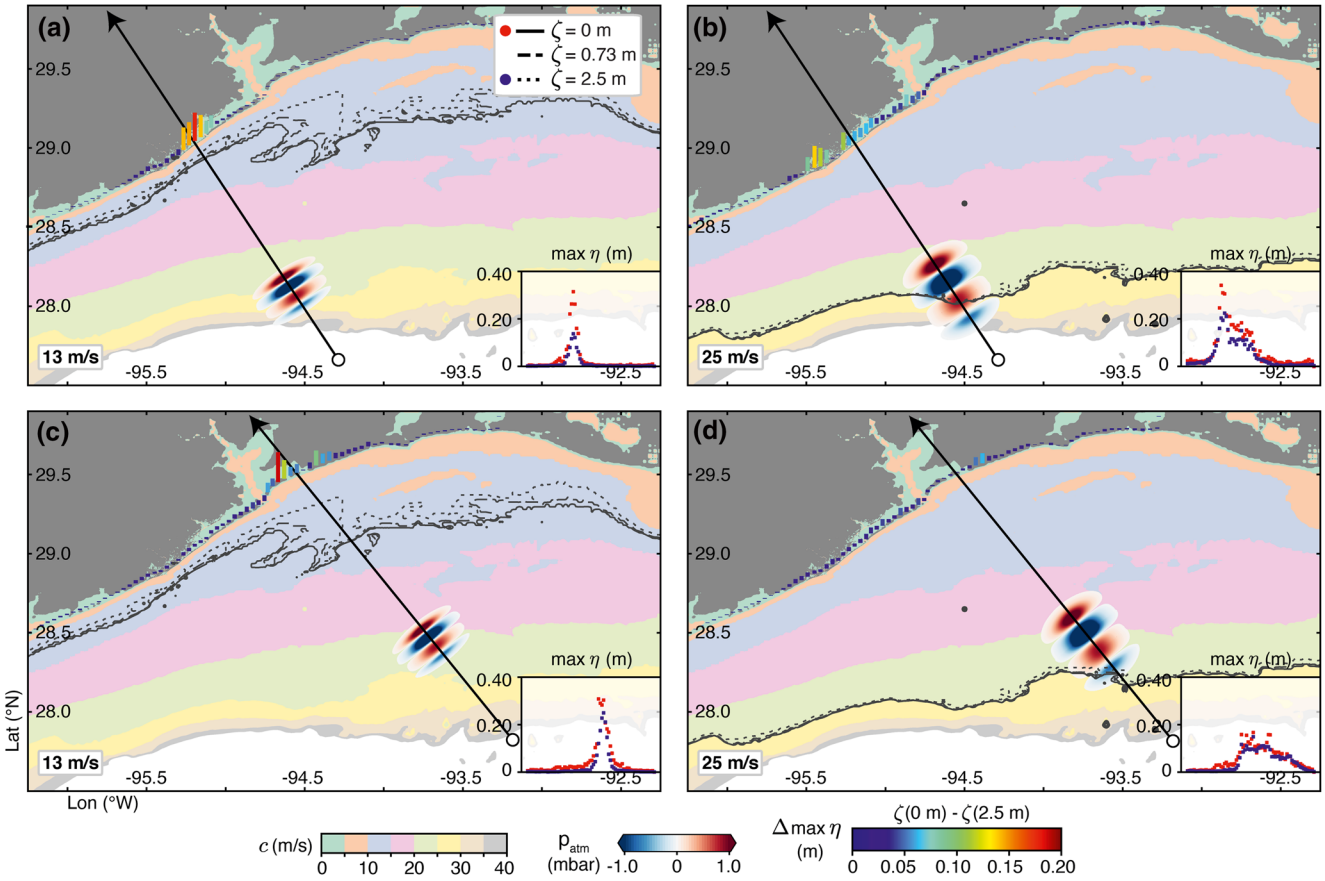

Figure 7. Sensitivity of meteotsunami generation, amplification, and propagation to storm surge ζ for the "landfall" air pressure disturbance, simulated with variable TCR forward speeds (a,c: 13 m/s, b,d: 25 m/s) and offshore bathymetry (a-b: original Follets Island landfall location, c-d: landfall shifted 80 km to the northeast). Meteotsunami generation varies with surge via the location of Proudman resonance (bold and dashed contour lines). Changes in meteotsunami amplification and propagation are depicted by the vertical colored bars which show the difference in the maximum sea-level anomaly η between the case of no surge and the largest simulated surge (2.5 m) along the entire coastline, with the maximum values for each scenario shown in the subplots for direct comparison.

and 0.73 m, respectively (Fleming et al., 2008). In contrast, during Hurricane Ike in 2008, storm surge measured 2.6 m at Follets Island (Harter & Figlus, 2017). The effect of storm surge on meteotsunami generation is to increase water depth and thereby move the location of Proudman resonance landward. In Figure 7, we show how this effect influences meteotsunami amplification and propagation for the "landfall" air pressure disturbance—both at the original Follets Island landfall location (Figures 7a and 7b) and 80 km to the northeast where the continental shelf is wider (Figures 7c and 7d)—by imposing a larger surge of 2.5 m (via an increase in still water). The vertical colored bars in each pane of Figure 7 show the difference in the maximum sea-level anomaly between the case of zero surge and the 2.5 m surge scenario along the entire coastline for each simulation. The effect of surge on meteotsunami amplification and propagation is complex, and varies both with the forward translation speed of the air pressure disturbance as well as the offshore bathymetry and shelf morphology. For example, comparing Figures 7a and 7b, the effect of an increase in surge on meteotsunami hazard (via an increase in the maximum sea-level anomaly at the coast) is larger for a relatively slow-moving air pressure disturbance (13 m/s) than for a relatively fast moving disturbance (25 m/s) along the original Follets Island trajectory. Although the meteotsunami surge response is also sensitive to changes in forward speed farther up the coast (Figures 7c and 7d), comparison of the two landfall locations shows that the decrease in meteotsunami hazard with an increase in surge is larger at Follets Island due to a slightly steeper sloping continental shelf (i.e., narrower meteotsunami enhancement region).

4. Discussion

Many of the VLF sea-level anomalies observed in the nearshore environment along the upper Texas Gulf coast during Hurricane Harvey appear to be meteotsunami initiated by TCRs distant from the storm center. This is evidenced by concurrent observations of large air pressure disturbances (peak or trough amplitudes > |±1.25| mbar) and high radar reflectivity—collectively indicating passage of TCRs and embedded convective cells (heavy precipitation, >∼50 dBZ) over the Follets Island field site—subsequent to arrival of relatively large VLF oscillations (amplitudes > 0.16 m). We corroborate the findings of (Shi et al., 2020) that meteotsunami are common along open coasts during TCs, and likewise find that meteotsunami hazard can span several days before and after landfall (Figure 1c). Meteotsunami reached 0.42 m in height in the surf zone at Follets Island, with peak and trough amplitudes typically O(0.2 m); this variability constituted 23% of the total variance (and 78% in the back-barrier bay) and is significant for such small mean-water depths (1.3–1.8 m, Figure 1b). Hence, it is likely that meteotsunami influenced shoreline motions and the extent of wave runup along this stretch of coastline. VLF sea-level anomalies were also observed during storm-driven overwash at Matagorda Peninsula, a barrier peninsula located ∼85 km southwest of Follets Island and closer to storm landfall. Anarde et al. (2020) hypothesize that these VLF sea-level anomalies are likewise meteotsunami triggered by TCRs, and using field data show that the slow variation of total water depth associated with this phenomenon slightly modulate infragravity wave heights during overwash. Although meteotsunami can clearly modify storm processes in very shallow water, it is unknown whether these waves are important contributors to sediment suspension and flux. A higher density of field measurements is needed to characterize meteotsunami transformation in the nearshore and the relative contribution of this phenomena to morphological change (i.e., beach and dune erosion) during hurricane impact.

TCRs are known to be accompanied by both strong pressure and wind disturbances, and in some cases develop squall-line like characteristics including heavy (convective) precipitation and low-level wind convergence zones (Yu et al., 2018). Shi et al. (2020) identified squall-line like TCRs as the main trigger of meteotsunami at tide gauges and showed with an idealized coupled oceanic and atmospheric model (COAWST; Warner et al. (2010)) that wind stress divergence was the key atmospheric forcing mechanism for meteotsunami generation by TCRs. Air pressure fluctuations were shown to play a negligible role in meteotsunami generation and amplification beyond the several centimeter perturbations produced by the inverse barometer effect. In contrast, the numerical modeling conducted as part of this study shows that air pressure disturbances accompanying TCRs can initiate and resonantly amplify sea-level anomalies across the wide GOM shelf and in some cases produce meteotsunamis with similar periods O(20 min) and amplitudes O(0.2 m) as surf zone observations (Figures 5 and 6). One potentially important distinction between the modeling conducted by Shi et al. (2020) and this current study is the numerical resolution of large gradients in air pressure over short distances. The air pressure disturbances measured during Hurricane Harvey featured sharp changes in pressure over short distances, particularly for the "landfall" scenario where trough and crest wavelengths ranged between 6 and 16 km for the range of simulated forward speeds (Figure 6). In order to numerically resolve these short-wavelength air pressure disturbances and the ensuing meteotsunami waves, the hydrodynamic model used in this study needs to be forced with higher temporal and spatial resolution (at least 20 grid points per wavelength and a grid resolution of 6 arcseconds; ∼185 m) than used in previous studies (e.g., the 3 km grid spacing and 5 min temporal resolution of the Weather Research and Forecast model used by Shi et al., 2020). By linking temporally high-resolution air pressure measurements with a high resolution grid, we find that sea-level anomalies forced by even relatively small pressure trough amplitudes (−1 mbar) can undergo large resonant amplification across the wide continental shelf ("early storm" simulation, Figure 5). For disturbances with larger and sharper pressure troughs (e.g., −2.8 mbar in the "landfall" simulations, Figure 6), simulated meteotsunami crest amplitudes can reach O(0.5 m) for certain forward speed scenarios and trajectories.

Although model simulations show that the measured air pressure disturbances during Hurricane Harvey can trigger meteotsunami similar to surf zone anomalies, this does not imply causality, and there are some important model simplifications, data-model differences, and uncertainties to consider in interpreting the model results. First, it is not clear in the scientific community if the atmospheric disturbances accompanying TCRs have the same length and shape as the radar reflectivity signal. Hence, the forward translation speeds of the air pressure disturbances used in model simulations, which are estimated from radar

reflectivity, may not be representative. While we can match the lag time between passage of the simulated air pressure trough and peak sea-level anomaly with that from observations (Figures 5b and 5f), we cannot confirm that the air pressure disturbance traveled at this speed over the region of wave amplification. Furthermore, we simplify the movement of the air pressure disturbance across the shelf by translating it at a constant speed and assume the pressure waveform does not change shape across the shelf (i.e., no convective modifications). For the "landfall" simulations, if the air pressure disturbance does follow the same path and translation speed as radar and indeed slows down when approaching land, it may be possible that multiple meteotsunamis can be generated by the same disturbance when it is moving fast far offshore (25 m/s) and slow-moving close to shore (13 m/s, Figure 6f). It is also known that the air pressure disturbances accompanying TCRs are significantly influenced by convective precipitation such that the troughs and peaks of air pressure couplets can both increase in amplitude or become undulated by moist convection (Yu & Tsai, 2010; Yu et al., 2018). Hence, it is likely that the air pressure waveform changes as it translates across the shelf, which could influence the characteristics of ensuing meteotsunami. Consistent with other numerical investigations of Proudman resonant wave growth, meteotsunami amplification, propagation, and therefore the spatial extent of meteotsunami hazard along the open coast is also sensitive to the length and trajectory of the air pressure disturbance (e.g., Ličer et al., 2017; Shi et al., 2020; Williams et al., 2020), particularly if the TCRs are fast-moving and forced waves thereby undergo resonance and become free waves far offshore (Figures 6c and 6e).

Given that radar reflectivity mosaics show that convective cells passed over much of the upper Texas coast throughout the storm (Figure 3), it may be that meteotsunami measured at Follets Island were generated by air pressure disturbances associated with convective cells that made landfall east of the field site. This could, for example, explain the data-model mismatch in meteotsunami period for the "early storm" simulation (Figure 5b), as well as observations of VLF sea-level anomalies following passage of this air pressure disturbance. However, the trajectory of the "early storm" TCR followed a slightly more radial path than simulated in Figures 5a and 5a radial trajectory for this air pressure disturbance and offshore bathymetry (traveling at 21 m/s) would only serve to increase the period of the meteotsunami observed at the coast due to an elongation of the "observed" pressure waveform over the region of resonance. An alternative hypothesis is that wind forcing triggered these early storm meteotsunami and is the source of the data-model mismatch in period. For TCRs that were large enough to pass over the neighboring Freeport tide gauge (Figures 3a and 3d), meteorological data show sudden changes in wind gust speed O(5–10 m/s) at similar intervals as the air pressure disturbances measured at Follets Island, both during early and late storm conditions (Figure 2f). Only a single sea-level anomaly of comparable magnitude to surf zone observations was measured at the Freeport tide gauge (0.35 m in peak-to-trough height, Figure 2b) and this oscillation was coincident with a sharp increase in wind gust speed (measuring 17 m/s, Figure 1f) as a TCR traversed directly (and nearly perpendicular) over the harbor. The Freeport tide gauge did not measure any large fluctuation in air pressure during passage of this TCR, nor at any other time during the study period. Hence, it is likely that wind forcing was the key atmospheric forcing mechanism for this sea-level anomaly. Given the orientation of the harbor jetties, it may be that meteotsunami propagation into this sheltered harbor requires normal incidence, a hypothesis that should be explored further through numerical modeling.

Numerical simulations also showed that meteotsunami hazard can additionally depend on the magnitude of storm surge, which acts to move the location of Proudman resonance—for both wind or air pressure disturbances—landward (Figure 7). For the atmospheric (TCR structure, forward speed, path of translation) and oceanographic (bathymetric configuration) conditions explored in this study, an increase in storm surge results in a decrease in meteotsunami hazard. These numerical results suggest that along this open coastline, meteotsunami hazard is largest for relatively low surge events, like Hurricane Harvey. It is unknown how increases in model complexity to incorporate additional oceanographic (astronomical tides and currents) and atmospheric factors (radial translation of disturbance, variable forward translation speed, temporal-modifications to the air pressure waveform, wind forcing) will effect meteotsunami hazard, and therefore the relative effect of storm surge for the cases simulated here. Lastly, the period and waveform of an air pressure disturbance accompanying a TCR as measured at a fixed point are related to the structure and orientation of the TCR and smaller convective cells. Therefore, the characteristics of the air pressure disturbances observed at Follets Island during Hurricane Harvey are site and storm specific. Given the sensitivity of simulated meteotsunami hazard to the atmospheric factors described in this study—including

the shape (amplitude, period), length, forward translation speed, and trajectory of the air pressure disturbance—as well as storm surge, efforts to produce forecasts of meteotsunami hazard by individual TCRs would be challenging.

5. Conclusions

Measurements of sea level along the upper Texas coast during Hurricane Harvey revealed that ocean waves with periods in the meteotsunami frequency band (~8–45 min periods) were common on both the sea and bay sides of a barrier island before, during, and after storm landfall. Radar reflectivity showed that the largest sea-level anomalies (measuring ~0.4 m in height in the surf zone) were proceeded by spiral rainbands. Sudden changes in wind speed and air pressure that accompany TCRs are known to trigger meteotsunamis. Previous (idealized) modeling has suggested that wind forcing is the dominant forcing mechanism for TCR-induced meteotsunami, with minor (several centimeters) contributions from fluctuations in air pressure. In contrast, the numerical modeling conducted as part of this study shows that measured air pressure disturbances accompanying TCRs during Hurricane Harvey have the potential to generate meteotsunamis with crests O(0.5 m), but meteotsunami amplification and propagation is sensitive to oceanographic (storm surge) and atmospheric factors (pressure waveform), including model uncertainties (length, forward translation speed, and trajectory of the air pressure disturbance). We find that for certain forward speeds and trajectories, large changes in air pressure (~1–3 mbar) can initiate and resonantly amplify sea-level anomalies across the wide continental shelf and produce meteotsunami with similar periods (~20 min) and amplitudes (~0.2 m) as surf zone observations. The measured air pressure disturbances often featured large gradients in air pressure over short distances (several to tens of kilometers), necessitating a numerical model with high temporal and spatial resolution to resolve short-wavelength air pressure forcing and the ensuing meteotsunami wave. Although we find the potential for meteotsunami generation by air pressure forcing, this does not imply causality; sudden and large changes in wind gust speed O(5–10 m/s) were also detected at regional tide gauges at similar intervals as the air pressure disturbances. More high resolution field and modeling studies are needed to ascertain the relative importance of wind and air pressure forcing for meteotsunami generation by TCRs for different coastal bathymetries and storm characteristics.

Data Availability Statement

The data can be obtained via the DesignSafe-CI Data Depot: https://doi.org/10.17603/ds2-m0bc-n829.

Acknowledgments
We thank Maitane Olabarrieta for her insightful comments that greatly strengthened this study, and all members of the COASTRR team for their assistance in the field during harsh conditions. We also thank Mick Prouse for his dedication and effort throughout the project. Funding was provided by the National Science Foundation (NSF) under grant No. OCE-1760713, an Institutional Grant (NA14OAR4170102) to the Texas Sea Grant College Program from the National Sea Grant Office, National Oceanic and Atmospheric Administration. Dr. Figlus received additional support under NSF grant No. OISE-1545837. All views, opinions, findings, conclusions, and recommendations expressed in this material are those of the authors and do not necessarily reflect the opinions of the funding agencies. Further support was provided by Texas A&M University at Galveston and the SSPEED Center at Rice University. Dr. Anarde was additionally supported by the Link Ocean Engineering and Instrumentation PhD Fellowship Program during this project.

References

Amante, C., & Eakins, B. (2009). *ETOPO1 1 arc-minute global relief model: Procedures, data sources and analysis*, Boulder, CO: (NOAA Technical Memorandum NESDIS NGDC-24): National Geophysical Data Center, NOAA. https://doi.org/10.7289/V5C8276M

Anarde, K., Figlus, J., Sous, D., & Tissier, M., & et al. (2020). Transformation of infragravity waves during hurricane overwash. *Journal of Marine Science and Engineering*, *8*(8), 545. https://doi.org/10.3390/jmse8080545

Churchill, D. D., Houston, S. H., & Bond, N. A. (1995). The Daytona Beach wave of 3–4 July 1992: A shallow-water gravity wave forced by a propagating squall line. *Bulletin of the American Meteorological Society*, *76*(1), 21–32. https://doi.org/10.1175/1520-0477(1995)076<0021:tdbwoj>2.0.co;2

Diercks, J. W., & Anthes, R. A. (1976). Diagnostic studies of spiral rainbands in a nonlinear hurricane model. *Journal of the Atmospheric Sciences*, *33*(6), 959–975. https://doi.org/10.1175/1520-0469(1976)033<0959:DSOSRI>2.0.CO;2

Dusek, G., DiVeglio, C., Licate, L., Heilman, L., Kirk, K., Paternostro, C., & Miller, A. (2019). A meteotsunami climatology along the U.S. East Coast. *Bulletin of the American Meteorological Society*, *100*(7), 1329–1345. https://doi.org/10.1175/BAMS-D-18-0206.1

Fleming, J. G., Fulcher, C. W., Luettich, R. A., Estrade, B. D., Allen, G. D., & Winer, H. S. (2008). *A real time storm surge forecasting system using ADCIRC*. Proceedings of the 10th International Conference on Estuarine and Coastal Modeling, Newport, Rhode Island (pp. 893–912).

Haller, M. C., Putrevu, U., Oltman-Shay, J., & Dalrymple, R. A. (1999). Wave group forcing of low frequency surf zone motion. *Coastal Engineering Journal*, *41*(2), 121–136. https://doi.org/10.1142/S0578563499000085

Hamuro, M., Kawata, Y., Matsuda, S., Matusno, T., Nakamura, N., Pak, T., et al. (1969). Precipitation bands of Typhoon Vera in 1959 (part I). *Journal of the Meteorological Society of Japan. Ser. II*, *47*(4), 298–309. https://doi.org/10.2151/jmsj1965.47.4_298

Harter, C., & Figlus, J. (2017). Numerical modeling of the morphodynamic response of a low-lying barrier island beach and foredune system inundated during Hurricane Ike using XBeach and CSHORE. *Coastal Engineering*, *120*, 64–74. https://doi.org/10.1016/j.coastaleng.2016.11.005

Hence, D. A., & Houze, R. A., Jr (2008). Kinematic structure of convective-scale elements in the rainbands of hurricanes katrina and rita (2005). *Journal of Geophysical Research*, *113*(D15). https://doi.org/10.1029/2007jd009429

Kim, S.-Y., Chun, H.-Y., & Wu, D. L. (2009). A study on stratospheric gravity waves generated by typhoon ewiniar: Numerical simulations and satellite observations. *Journal of Geophysical Research*, *114*(D22). https://doi.org/10.1029/2009jd011971

Kowalik, Z., Knight, W., Logan, T., & Whitmore, P. (2005). Numerical Modeling of the Global Tsunami: Indonesian Tsunami of 26 December 2004. *Science of Tsunami Hazards*, *23*(1), 40–56.

Kurihara, Y. (1976). On the development of spiral bands in a tropical cyclone. *Journal of the Atmospheric Sciences*, *33*(6), 940–958. https://doi.org/10.1175/1520-0469(1976)033<0940:otdosb>2.0.co;2

Ličer, M., Mourre, B., Troupin, C., Krietemeyer, A., Jansá, A., & Tintoré, J. (2017). Numerical study of Balearic meteotsunami generation and propagation under synthetic gravity wave forcing. *Ocean Modelling*, *111*, 38–45. https://doi.org/10.1016/j.ocemod.2017.02.001

Ligda, M. G. (1955). Hurricane Squall Lines. *Bulletin of the American Meteorological Society*, *36*(7), 340–342. https://doi.org/10.1175/1520-0477-36.7.340

Linares, Á., Wu, C. H., Bechle, A. J., Anderson, E. J., & Kristovich, D. A. (2019). Unexpected rip currents induced by a meteotsunami. *Scientific Reports*, *9*(1), 1–9. https://doi.org/10.1038/s41598-019-38716-2

Lin, L.-C., & Wu, C. H. (2020). Unexpected meteotsunamis prior to typhoon wipha and typhoon neoguri. *Natural Hazards*, 1–14. https://doi.org/10.1007/s11069-020-04313-0

Mecking, J., Fogarty, C., Greatbatch, R., Sheng, J., & Mercer, D. (2009). Using atmospheric model output to simulate the meteorological tsunami response to Tropical Storm Helene (2000). *Journal of Geophysical Research*, *114*(C10). https://doi.org/10.1029/2009JC005290

Mercer, D., Sheng, J., Greatbatch, R. J., & Bobanović, J. (2002). Barotropic waves generated by storms moving rapidly over shallow water. *Journal of Geophysical Research*, *107*(C10), 16-1. https://doi.org/10.1029/2001JC001140

Monserrat, S., Vilibić, I., & Rabinovich, A. (2006). Meteotsunamis: Atmospherically induced destructive ocean waves in the tsunami frequency band. *Natural Hazards and Earth System Science*, *6*(6), 1035–1051. https://doi.org/10.5194/nhess-6-1035-2006

NCEI. (2015). *Digital elevation models for the U.S. Coast, NESDIS, NOAA*. Boulder, CO: U.S. Department of Commerce. Retrieved from https://www.ngdc.noaa.gov/thredds/catalog/tiles/tiled_19as/catalog.html

NCEI-NOAA. (2019). *Radar data map*. Retrieved from https://gis.ncdc.noaa.gov/maps/ncei/radar

NOAA. (2017). *Freeport SPIP, Freeport Harbor, TX—Station ID: 8772471*. Retrieved from https://tidesandcurrents.noaa.gov/stationhome.html?id=8772471

Nolan, D. S., & Zhang, J. A. (2017). Spiral gravity waves radiating from tropical cyclones. *Geophysical Research Letters*, *44*(8), 3924–3931. https://doi.org/10.1002/2017GL073572

Olabarrieta, M., Valle-Levinson, A., Martinez, C. J., Pattiaratchi, C., & Shi, L. (2017). Meteotsunamis in the northeastern Gulf of Mexico and their possible link to El Niño Southern Oscillation. *Natural Hazards*, *88*(3), 1325–1346. https://doi.org/10.1007/s11069-017-2922-3

Oltman-Shay, J., Howd, P., & Birkemeier, W. (1989). Shear instabilities of the mean longshore current: 2. Field observations. *Journal of Geophysical Research*, *94*(C12), 18031–18042. https://doi.org/10.1029/jc094ic12p18031

Proudman, J. (1929). The effects on the sea of changes in atmospheric pressure. *Geophysical Journal International*, *2*, 197–209. https://doi.org/10.1111/j.1365-246X.1929.tb05408.x

Rabinovich, A. B. (2020). Twenty-seven years of progress in the science of meteorological tsunamis following the 1992 Daytona Beach event. *Pure and Applied Geophysics*, *177*(3), 1193–1230. https://doi.org/10.1007/s00024-019-02349-3

Shi, L., Olabarrieta, M., Nolan, D. S., & Warner, J. C. (2020). Tropical cyclone rainbands can trigger meteotsunamis. *Nature Communications*, *11*(1), 1–14. https://doi.org/10.1038/s41467-020-14423-9

Shi, L., Olabarrieta, M., Valle-Levinson, A., & Warner, J. C. (2019). Relevance of wind stress and wave-dependent ocean surface roughness on the generation of winter meteotsunamis in the Northern Gulf of Mexico. *Ocean Modelling*, 101408.*140*, https://doi.org/10.1016/j.ocemod.2019.101408

Ushijima, T. (1958). Outer rain bands of typhoons. *Journal of the Meteorological Society of Japan. Ser. II*, *36*(1), 1–10.

Wang, Y. (2009). How do outer spiral rainbands affect tropical cyclone structure and intensity? *Journal of the Atmospheric Sciences*, *66*(5), 1250–1273. https://doi.org/10.1175/2008JAS2737.1

Warner, J. C., Armstrong, B., He, R., & Zambon, J. B. (2010). Development of a coupled ocean–atmosphere–wave–sediment transport (coawst) modeling system. *Ocean Modelling*, *35*(3), 230–244. https://doi.org/10.1016/j.ocemod.2010.07.010

Williams, D. A., Horsburgh, K. J., Schultz, D. M., & Hughes, C. W. (2020). Proudman resonance with tides, bathymetry and variable atmospheric forcings. *Natural Hazards*, 1–26. https://doi.org/10.1007/s11069-020-03896-y

Willoughby, H. (1977). Inertia-buoyancy waves in hurricanes. *Journal of the Atmospheric Sciences*, *34*(7), 1028–1039. https://doi.org/10.1175/1520-0469(1977)034<1028:ibwih>2.0.co;2

Yu, C.-K., Lin, C.-Y., Cheng, L.-W., Luo, J.-S., Wu, C.-C., & Chen, Y. (2018). The degree of prevalence of similarity between outer tropical cyclone rainbands and squall lines. *Scientific Reports*, *8*(1), 8247. https://doi.org/10.1038/s41598-018-26553-8

Yu, C.-K., & Tsai, C.-L. (2010). Surface pressure features of landfalling typhoon rainbands and their possible causes. *Journal of the Atmospheric Sciences*, *67*(9), 2893–2911. https://doi.org/10.1175/2010jas3312.1